Competition of disorder and electron-phonon coupling in $2H$-$TaSe_{2-x}S_x$ ($0 \leqslant x \leqslant 2$) as evidenced by Raman spectroscopy

J. Blagojević,[1] S. Djurdjić Mijin,[1,2] J. Bekaert,[3] M. Opačić,[1] Y. Liu,[4,5] M. V. Milošević,[3] C. Petrović,[4,6,7] Z. V. Popović,[8] and N. Lazarević[1]

[1]*Institute of Physics Belgrade, University of Belgrade, Pregrevica 118, 11080 Belgrade, Serbia*
[2]*Departamento de Física de Materiales, Facultad de Ciencias, Universidad Autónoma de Madrid, 28049 Madrid, Spain*
[3]*Department of Physics & NANOlab Center of Excellence, University of Antwerp, Groenenborgerlaan 171, B-2020 Antwerp, Belgium*
[4]*Condensed Matter Physics and Material Science Department, Brookhaven National Laboratory, Upton, New York 11973-5000, USA*
[5]*Center for Correlated Matter and School of Physics, Zhejiang University, Hangzhou 310058, People's Republic of China*
[6]*Shanghai Key Laboratory of Material Frontiers Research in Extreme Environments (MFree), Shanghai Advanced Research in Physical Sciences (SHARPS), Pudong, Shanghai 201203, China*
[7]*Department of Nuclear and Plasma Physics, Vinca Institute of Nuclear Sciences, University of Belgrade, Belgrade 11001, Serbia*
[8]*Serbian Academy of Sciences and Arts, Knez Mihailova 35, 11000 Belgrade, Serbia*

(Received 16 November 2023; accepted 31 January 2024; published 21 February 2024)

The vibrational properties of $2H$-$TaSe_{2-x}S_x$ ($0 \leqslant x \leqslant 2$) single crystals were probed using Raman spectroscopy and density functional theory calculations. The end members revealed two out of four symmetry-predicted Raman active modes, together with the pronounced two-phonon structure, attributable to the enhanced electron-phonon coupling. Additional peaks become observable due to crystallographic disorder for the doped samples. The evolution of the E^2_{2g} mode Fano parameter reveals that the disorder has a weak impact on electron-phonon coupling, which is also supported by the persistence of two-phonon structure in doped samples. As such, this research provides thorough insights into the lattice properties, the effects of crystallographic disorder on Raman spectra, and the interplay of this disorder with the electron-phonon coupling in $2H$-$TaSe_{2-x}S_x$ compounds.

DOI: 10.1103/PhysRevMaterials.8.024004

I. INTRODUCTION

Transition metal dichalcogenides, a well studied family of quasi-2D materials, have attracted considerable attention in the recent years due to their rich phase diagrams, thickness-dependent transport, unique optical properties and collective electron phenomena (e.g., charge density waves and superconductivity) [1–5]. Since the experimental confirmation of the coexistence of superconductivity (SC) and charge density waves (CDW) transition metal dichalcogenides have established themselves as the ideal candidates for their investigation, given that these phenomena arise at experimentally accessible temperatures in them [6–8].

Previous experimental research has shown that at room temperature both $2H$-TaS_2 and $2H$-$TaSe_2$ crystallize into the hexagonal structure, described by the space group $P6_3/mmc$ (D_{6h}) [9,10]. The opulent phase diagram of $2H$-$TaSe_2$ includes numerous charge density wave (CDW) phases at high temperatures—the incommensurate CDW (ICCDW) phase at $T_{1C} = 122$ K, the single commensurate CDW (SCCDW) phase in the temperature range from $T_{\downarrow 2C} = 112$ K to $T_{\uparrow 2C} = 90$ K, and the triply commensurate (TCCDW) phase at $T_{3C} = 90$ K [9–12]. As for $2H$-TaS_2, transition from the normal (metallic) to the ICDW phase occurs at $T_{\mathrm{CDW}} = 78$ K [13]. These materials exhibit unusually large Raman two-phonon scattering cross section, often correlated with the existence of CDW phase [10,13–15]. Two-phonon feature in $2H$-TaS_2 was attributed to second-order scattering of acoustic and quasi-acoustic modes near the $q_{\mathrm{CDW}} \cong \frac{2}{3}\Gamma\mathrm{M}$ [16].

The latest experimental results indicate that the substitution of Se atoms with S atoms leads to a weak double dome evolution of the superconducting critical temperature T_{SC}. The T_{SC} dependence coincides with the evolution of crystallographic disorder, suggesting that the crystalline disorder favors superconductivity while suppressing the CDW phase [17]. Similarly, other types of disorder generated by etching nanopores in monolayer TaS_2 sheets [18], or by spontaneous filling of vacant sulfur sites by oxygen in few-layer $2H$-TaS_2 samples [19] enhance superconductivity in this system. In addition, first-principles calculations have revealed that the electron-phonon coupling within TaS_2 sheets is drastically boosted (by oxygenation up to 80%) [19], providing additional pathway to enhance superconductivity by doping, while suppressing the CDW state.

In this work, we present a Raman spectroscopy study of $2H$-$TaSe_{2-x}S_x$ ($0 \leqslant x \leqslant 2$) alloys. Obtained experimental results were found to be in good agreement with the density functional theory (DFT) calculations. The experimental Raman spectra of the end compounds host two out of the four symmetry-predicted Raman active modes. Additionally, a low-intensity overtone peak O_1 obeying pure A_{1g} selection rules can be observed only in the spectra of $2H$-TaS_2. The origin of the two-phonon structure is attributed to enhanced electron-phonon coupling within phonon branches around the

M and L points. In the spectra of doped samples additional peak and a dynamic evolution of the two-phonon structure are observed due to crystallographic disorder. Our analysis of the inverse Fano parameter $1/|q|$ of E_{2g}^2 mode indicates a weak impact of crystallographic disorder on electron-phonon coupling.

II. EXPERIMENTAL AND COMPUTATIONAL DETAILS

The preparation of the single crystal $2H$-$TaSe_{2-x}S_x$ alloys used in this study is described elsewhere [17]. The Raman experiment was performed using a Tri Vista 557 spectrometer with a 1800/1800/2400 grooves/mm diffraction grating combination in a backscattering configuration. As an excitation source, the 514 nm line of a Coherent Ar^+/Kr^+ ion laser was used. The direction of the incident (scattered) light coincides with the crystallographic c axis. Laser beam focusing was achieved through a microscope objective with 50× magnification. During the measurements the samples were placed inside of a KONTI CryoVac continuous helium flow cryostat with 0.5-mm-thick window. All samples were cleaved in the air before being placed into the cryostat. The obtained Raman spectra were corrected by the Bose factor and presented with linear scale. The spectrometer resolution is comparable to the Gaussian width of 1 cm^{-1}. Next, we have performed density functional theory (DFT) calculations as implemented in the ABINIT package [20]. We have used the Perdew-Burke-Ernzerhof (PBE) functional, an energy cutoff of 50 Ha for the plane wave basis, and included spin-orbit coupling by means of fully relativistic Goedecker pseudopotentials [21,22], where Ta-$5d^36s^2$, S-$3s^23p^4$, and Se-$4s^24p^4$ states are treated as valence electrons. The crystal structure was relaxed so that forces on each atom were below 0.05 meV/Å and the total stress on the unit cell below 0.1 bar. This relaxation yields lattice parameters $a = 3.39$ Å, $c = 14.00$ Å for TaS_2 and $a = 3.51$ Å, $c = 14.37$ Å for $TaSe_2$. Subsequently, the phonons and the electron-phonon coupling (EPC) were obtained from density functional perturbation theory (DFPT) calculations, also within ABINIT [23]. Here, we have used a 16×16×6 **k**-point grid for the electron wave vectors and an 8×8×3 **q**-point grid for the phonon wave vectors. For the electronic occupation, we employed Fermi-Dirac smearing with broadening factor $\sigma_{FD} = 0.01$ Ha (sufficiently high to exclude unstable phonon modes related to the low-temperature CDW phases).

The phonon-wave-vector (**q**)- and mode(ν)-resolved electron-phonon coupling, plotted in Fig. 2, was evaluated as

$$\lambda_{\mathbf{q}\nu} = \frac{2}{N_F \omega_{\mathbf{q}\nu}} \sum_{\mathbf{k},n,m} \left| g^{\nu}_{\mathbf{k}n,\mathbf{k}+\mathbf{q}m} \right|^2 \delta(\varepsilon_{\mathbf{k}n} - \varepsilon_F)\delta(\varepsilon_{\mathbf{k}+\mathbf{q}m} - \varepsilon_F),$$

where N_F is the electronic density of states at the Fermi level (ε_F), $\omega_{\mathbf{q}\nu}$ are the phonon frequencies, $g^{\nu}_{\mathbf{k}n,\mathbf{k}+\mathbf{q}m}$ the electron-phonon coupling matrix elements obtained from DFPT calculations, with n and m electronic band indices, and $\varepsilon_{\mathbf{k}n}$ ($\varepsilon_{\mathbf{k}+\mathbf{q}m}$) the electronic eigenvalue for band n (m) and electronic wave vector **k** (**k**+**q**) obtained from DFT calculations.

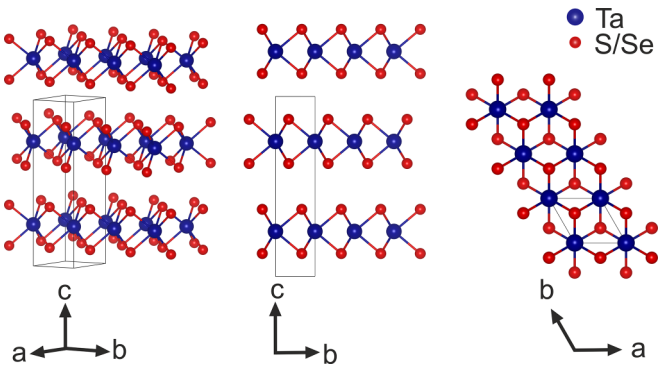

FIG. 1. Schematic representation of crystal structure of $2H$-$TaSe_2$ ($2H$-TaS_2) in various orientations.

III. RESULTS AND DISCUSSION

A. $2H$-$TaSe_2$ and $2H$-TaS_2

All single crystal alloys of $2H$-$TaSe_{2-x}S_x$ ($0 \leqslant x \leqslant 2$) crystallize into $P6_3/mmc$ crystal structure (Fig. 1) [9,10]. Wyckoff positions of atoms and their contributions to the Γ-point phonons together with corresponding Raman tensors for the two end compounds are listed in Table I. In total, the symmetry analysis predicts four Raman-active modes ($A_{1g} + E_{1g} + 2E_{2g}$) for the two end compounds of $2H$-$TaSe_{2-x}S_x$. According to the Raman tensors presented in Table I, A_{1g} modes can be observed only in parallel polarization configuration, whereas E_{2g} modes can be observed in spectra measured both in parallel and crossed polarization configurations. For our backscattering configuration, where laser beam is focused along the c axis onto the ab plane, the E_{1g} mode is unobservable.

Raman spectra of the two end compounds $2H$-$TaSe_2$ and $2H$-TaS_2 measured at $T = 150$ K are presented in Figs. 2(a) and 2(c), respectively. This particular temperature has been chosen because it is significantly higher than the critical temperature of the CDW phase transitions. The Raman

TABLE I. Wyckoff positions of atoms and their contributions to the Γ-point Raman active phonons for the $P6_3/mmc$ space group of $2H$-$TaSe_2$ (and $2H$-TaS_2) together with the corresponding Raman tensors.

Space group: $P6_3/mmc$ (194)	
Atoms	Irreducible representations
Ta ($2b$)	E_{2g}
Se/S ($4f$)	$A_{1g} + E_{1g} + E_{2g}$
Raman tensors	

$$A_{1g} = \begin{pmatrix} a & 0 & 0 \\ 0 & a & 0 \\ 0 & 0 & b \end{pmatrix}$$

$$^1E_{1g} = \begin{pmatrix} 0 & 0 & 0 \\ 0 & 0 & c \\ 0 & c & 0 \end{pmatrix} \quad ^2E_{1g} = \begin{pmatrix} 0 & 0 & -c \\ 0 & 0 & 0 \\ -c & 0 & 0 \end{pmatrix}$$

$$^1E^2_{2g} = \begin{pmatrix} d & 0 & 0 \\ 0 & -d & 0 \\ 0 & 0 & 0 \end{pmatrix} \quad ^2E^2_{2g} = \begin{pmatrix} 0 & -d & 0 \\ -d & 0 & 0 \\ 0 & 0 & 0 \end{pmatrix}$$

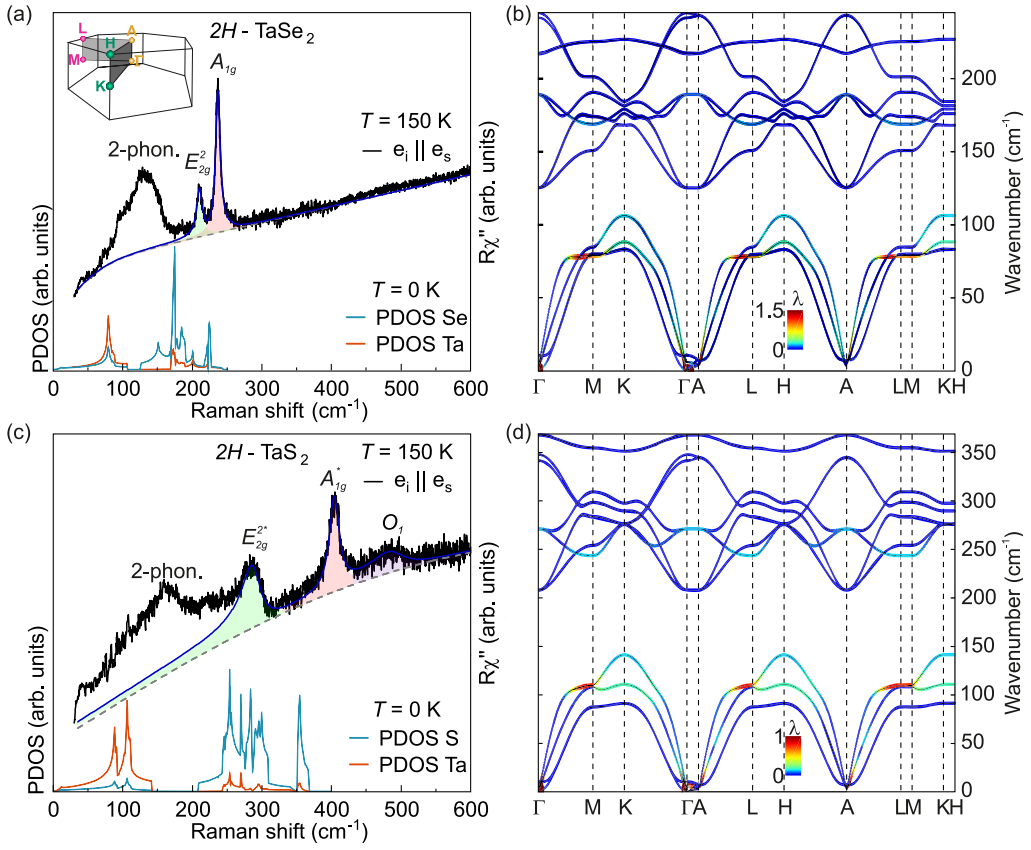

FIG. 2. [(a) and (c)] Raman response of $2H$-$TaSe_2$ and $2H$-TaS_2 for parallel polarization configuration at $T = 150$ K. The blue solid line represents the cumulative fit consisting of electronic continuum (dashed line) and phonon modes. The electronic continuum was modeled using simplified approach as described in [24], utilizing the following function: $R''_\chi(\omega, T) = a(T)\tanh\frac{\omega}{c(T)} + b(T)\frac{\omega}{c(T)}$. Here $a(T)$, $b(T)$, and $c(T)$ are temperature dependent parameters determined for each sample. Phonon modes were fitted using Fano line profile. Parts of spectra not covered by cumulative fit were identified to originate from two-phonon scattering. The contributions of the Ta (orange) and Se/S atoms (blue) to the calculated PDOS are shown as insets. First Brillouin zone with indicated points and lines of high symmetry is also shown in the inset of (a). [(b) and (d)] The calculated phonon dispersion of corresponding pure samples in the normal phase, with the value of electron-phonon coupling constant (λ) indicated through the color scale.

spectra of the pristine samples exhibit two prominent peaks, assigned as A_{1g} and E^2_{2g} symmetry modes, accompanied by a broad structure and an additional peak in the case of $2H$-TaS_2. For clarity, Raman-active modes observed in $2H$-TaS_2 spectra are marked with asterisk. Theoretically predicted modes are first analyzed, after which we address the origin and nature of additional peak and broad structure. The Raman responses of both samples were analyzed with a cumulative fit to include electronic continuum and discrete single-phonon excitations. The Breit-Wigner-Fano profile was used to model single-phonon excitations, due to visible asymmetry of the E^2_{2g} modes. For simplicity, the A_{1g} modes were fitted with constant Fano parameter $|q| = 50$, as they are highly symmetric. The phonon energies obtained in this way, alongside the calculated ones are listed in Table II. The lower frequency E^1_{2g} modes are related to shear (S) movements of the layers, with frequencies of $\sim$5 cm^{-1} for both compounds, whereas B^1_{1g} modes represent the layer breathing (LB) and are expected at frequencies $\sim$10 cm^{-1}.\

As can be seen in Table II, the discrepancy in experimental and theoretical phonon energy is less than 10% for all observed modes. The E^1_{2g} modes were not observed in the investigated energy region in accordance to our numerical calculations and are not in the focus of this study. The phonon dispersions, obtained from the DFPT calculations, are shown in Figs. 2(b) and 2(d), together with the calculated values of the EPC constant λ. These indicate the presence of nonzero EPC in E^2_{2g} scattering channel, giving rise to asymmetric line profiles. On the other hand in the A_{1g} channel no EPC was found, thus they should have symmetric profiles, as we have observed.

In addition to the observed Raman-active modes, the spectra of $2H$-TaS_2 in the parallel polarization configuration host the O_1 peak, with energy at about $\sim$490 cm^{-1}. This peak cannot be explained in terms of the first-order Raman scattering as its energy is well beyond the phonon energy range [see Fig. 2(d)]. Despite this, we have included this peak in the cumulative fit in order to track its energy. Previously reported large two-phonon scattering cross section in this material [10,13–16] indicates a second-order Raman scattering, which might occur due to defect and/or enhanced EPC. The absence of additional first-order peaks at energies with the highest phonon density of states (PDOS) values contradicts the expectations for defect-induced peaks [25]. Considering that one of the PDOS maxima ($\sim$250 cm^{-1}) is located near the energies that correspond to the half energy of O_1 peak

TABLE II. Phonon symmetries and phonon energies (in units of cm^{-1}) at Γ and their degeneracies for the $P6_3/mmc$ structure of $2H$-TaS_2 and $2H$-$TaSe_2$. The experimental values were determined at 300 K with experimental uncertainty of 0.3 cm^{-1}. The DFPT calculations were performed at zero temperature. In case of the lowest two modes, "S" stands for shear and "LB" for layer breathing.

		$2H$-TaS_2		$2H$-$TaSe_2$	
Symm.	Deg.	Calc.	Exp.	Calc.	Exp.
E^1_{2g} (S)	2	4.9		5.5	
B^1_{1g} (LB)	1	10.4		10.7	
E_{2u}	2	208.0		125.4	
E_{1g}	2	208.1		125.4	
E^2_{2g}	2	271.3	288.8	189.1	207.7
E_{1u}	2	271.3		189.2	
A_{2u}	1	341.6		241.8	
B^2_{1g}	1	348.0		245.1	
B_{1u}	1	368.0		216.9	
A_{1g}	1	368.5	402.9	217.7	234.7

[Fig. 2(c)], we believe that this peak is an overtone in nature and is observable due to enhanced EPC. To determine the validity of this assumption, the phonon dispersion curves and electron-phonon coupling constant λ [Fig. 2(d)] were further examined. If the O_1 peak is, indeed, observable due to electron-phonon coupling, we would expect that optical phonon branches around energies $\omega_{O_1}/2$ express high values of λ. As it is indicated in Fig. 2(d), several optical branches along the lines of high symmetry, at energies just below 250 cm^{-1}, meet this condition thus supporting our assumption.

The broad structures in the spectra of $2H$-$TaSe_2$ and $2H$-TaS_2, with energies at about ∼130 and ∼160 cm^{-1}, respectively, are centered in the gap of the theoretical PDOS, thus not a result of the first-order Raman scattering. Considering previous discussion on the origin of the O_1 peak in $2H$-TaS_2 spectra and applying similar analysis, these structures can likewise be explained as a two-phonon processes, predominantly overtones in nature but also with combinations contribution (as can be deduced from Fig. 5), also originating from the enhanced electron-phonon coupling. As shown in Fig. 2, peaks in PDOS values can be found in the $\omega_{2\text{phon}}/2$ energy ranges. By examining the phonon dispersion curves of $2H$-TaS_2 and $2H$-$TaSe_2$ (Fig. 2), several phonon branches with enhanced EPC are in the appropriate energy range for the two-phonon process. In the case of $2H$-TaS_2, these branches fall within the energy range of 100–150 cm^{-1}, while for $2H$-$TaSe_2$, they lie in the range of 50–100 cm^{-1}. It was reported in a previous study [16] that the origin of two-phonon structure in $2H$-TaS_2 is in the vicinity of the CDW wave vector $q_{\text{CDW}} \cong \frac{2}{3}\Gamma\text{M}$, where strong EPC exists. We argue that the origin of large scattering cross section for the two-phonon process is enhanced EPC in a much larger phase space that is required to reproduce the high Raman cross-section of the observed structures.

The phonon branches along (and in the vicinity) the lines of high symmetry: Γ-M, A-L, and L-M (illustrated in Fig. 2), demonstrate the highest values of the electron-phonon coupling constant, and we believe that these regions of phase space contribute to the two-phonon process. As anticipated, these branches closely coincide with energy levels that correspond to $\omega_{2\text{phon}}/2$, since the major contribution lies in the A_{1g} symmetry corresponding to the overtones (see Appendix A). This provides a strong argument to support our assumptions, regarding the nature and the origin of the two-phonon structures. Significantly higher intensity of the two-phonon structure in $2H$-TaS_2, compared to the O_1 peak, can be attributed to the stronger EPC observed in the corresponding phonon branches, as supported by our DFT calculations.

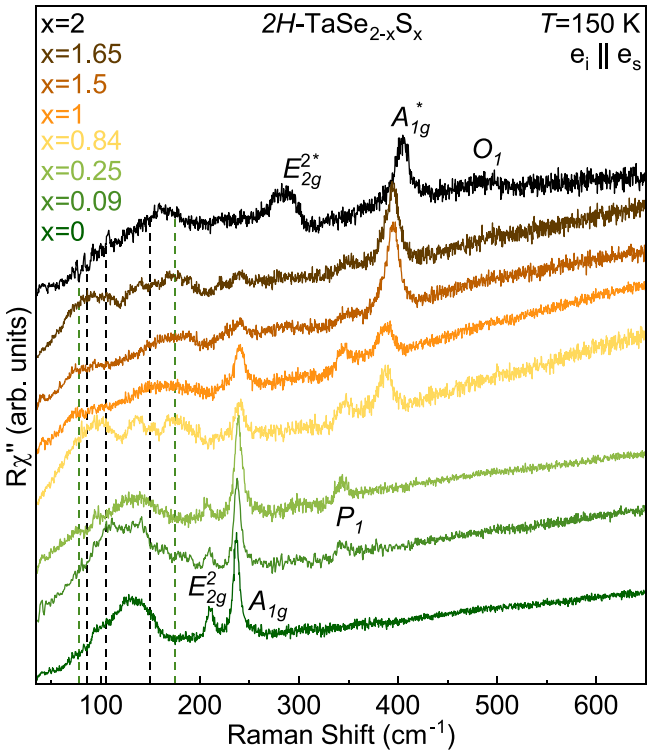

FIG. 3. Raman spectra of $2H$-$TaSe_{2-x}S_x$ measured at 150 K in parallel polarization configuration. Additionally to the A_{1g}, A^*_{1g}, E^2_{2g}, and E^{2*}_{2g} modes, one peak assigned as P_1 and PDOS projection onto two-phonon structure arise in the spectra of doped materials. With dashed lines are marked places of PDOS maxima in both pure samples. Spectra contain offset in y direction for clarity.

B. $2H$-$TaSe_{2-x}S_x$ ($0 \leqslant x \leqslant 2$)

Raman spectra of the $2H$-$TaSe_{2-x}S_x$ ($0 \leqslant x \leqslant 2$) single crystals measured in parallel polarization configuration at $T = 150$ K are presented in Fig. 3. The two modes that are present in the spectra of pristine $2H$-$TaSe_2$—A_{1g} and E^2_{2g}, can also be observed in the spectra of the doped samples. The A_{1g} symmetry mode persists in the spectra up to $2H$-TaSeS. As x increases further we cannot be certain that the existing feature in spectra is A_{1g} mode, because of low Se content and possible $2H$-TaS_2 PDOS contributions. Converesly, E^2_{2g} vanishes for $x = 0.84$, while A^*_{1g} and E^{2*}_{2g} modes can last be found in the spectra of $2H$-$TaSe_{1.16}S_{0.84}$ and $2H$-$TaSe_{0.5}S_{1.5}$, respectively. Considering that E^2_{2g} and E^{2*}_{2g} arise from the out-of-phase in-plane oscillations of Ta and Se/S atoms, the dependence on sulfur content x exhibits a discontinuous behavior. For

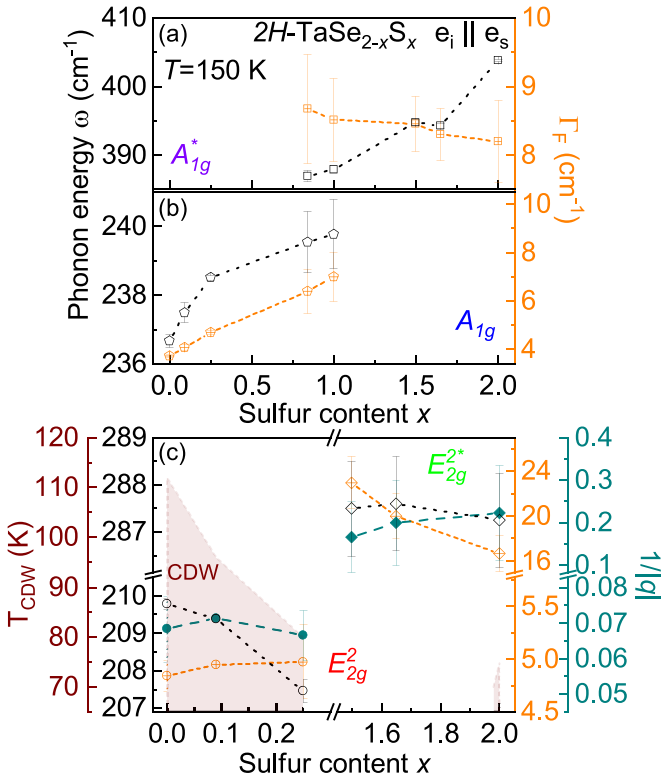

FIG. 4. The evolution of phonon energies (black) and line widths (orange) of the (a) A_{1g}^{*} and (b) A_{1g} Raman-active modes. (c) The evolution of phonon energies, line widths and inverse value of Fano parameter $1/|q|$ (teal) of the E_{2g}^{2*} and E_{2g}^{2} modes with the sulfur content x. T_{CDW} (dark red) dependence on the sulfur content x (obtained from electrical resistivity measurements presented in Ref. [17]), together with the electronic phase diagram (shaded red) of $2H$-$TaSe_{2-x}S_x$ reflect the evolution of crystallographic disorder.

the A_{1g} mode (out-of-plane movement of Se/S atoms), we observe continuous change with doping alongside simultaneous coexistence of A_{1g} and A_{1g}^{*} peaks in samples where Se/S concentration ratio is around unity. In the specific case of $2H$-TaSeS, at the nanoscale level, localized regions may emerge where either Se or S atoms predominate. Although these regions possess a sufficient size to generate detectable signals, they are significantly smaller in comparison to the laser spot ($\sim$5 μm^2), resulting in the inclusion of a considerable number of such clusters of atoms within the laser's spatial coverage. Consequently, the resulting Raman spectrum displays discernible contributions from both elements. The concentrations at which the E_{2g}^{2} mode vanishes directly correlate with disorder reaching its maximum value. Given that doping modifies the bond lengths of Ta-S and Ta-Se atoms, which, in conjunction with the accompanying lattice disorder, has a detrimental effect on the E_{2g}^{2} mode.

The gradual substitution of the selenium atoms with sulfur in the $2H$-$TaSe_2$ crystals introduces crystallographic disorder, giving rise to new scattering channels that result in additional peak observed in the Raman spectra of doped materials. This new peak with energy at about 342 cm^{-1}, assigned as P_1 is observed exclusively in doped spectra measured in parallel polarization configuration, therefore obeying A_{1g} symmetry rules. It is presumably an overtone mode, as its energy closely matches double that of the location where the highest PDOS value of the $2H$-$TaSe_2$ is situated.

To further investigate the effects of crystallographic disorder, we have inspected the evolution of phonon parameters with the sulfur content x, depicted in Fig. 4. As in the case of pure samples, all phonon lines were fitted using Fano profiles. No asymmetry was observed for the A_{1g} modes and they were fitted with the value of Fano parameter q being fixed at 50. All modes but E_{2g}^{2} harden with the increase in the sulfur concentration in the measured crystals. Given the difference in the atomic mass of Se and S and a reduction of the unit cell volume [17], one would expect that the E_{2g}^{2} mode also hardens with increasing x [26–28]. The unexpected behavior of E_{2g}^{2} mode might be attributed to the enhanced EPC, which potentially overcompensates previously mentioned effects. All Raman modes broaden due to increased crystallographic disorder. Considering that the Fano profiles are used to describe the line shape originating from coupling between phonon and electronic continuum, and that the Fano parameter depends on the interaction strength between the phonon and the continuum, the inverse value of Fano parameter $1/|q|$ can be used as a direct measure of the strength of EPC [29–32]. The interference of two-phonon structure in the fitting procedure produces large uncertainty [see Fig. 4(c)], preventing a clear assertion about the EPC, other than it persists through growing disorder. This result falls within the range of the potential increase in disorder-induced EPC [17].

Crystallographic disorder also has a significant impact on the evolution of two-phonon structure. Changing the sulfur content to $x = 0.09$, the broad structure in pristine $2H$-$TaSe_2$ spectra centered at around 130 cm^{-1} undergoes a further broadening accompanied by pronounced evolution of the shoulder at around $\sim$110 cm^{-1}, likely due to more pronounced evolution of the EPC in the related phonon branches. Raising the sulfur content to 0.25 and thus further increasing disorder restores the structure to a solitary broad peak. However, the most drastic change is observed in the spectra when $x = 0.84$, where four first order peaks are superimposed onto a broad two-phonon structure. As discussed previously, the additional peaks might become observable in Raman experiment due to defect scattering and are related to the regions where the PDOS reaches its maximum: at $\sim$90 cm^{-1} and $\sim$110 cm^{-1} for $2H$-TaS_2, at $\sim$80 cm^{-1} and $\sim$175 cm^{-1} for $2H$-$TaSe_2$ (see Fig. 2). These correspond rather well with the energies of the newly observed phonon modes. Raising the concentration of sulfur to $x = 1$ results in a wholly diluted structure consisting of two broad peaks at around $\sim$80 and $\sim$160 cm^{-1}. In the spectra with sulfur content $x = 1.65$, structure resembles that of the $x = 0.84$, albeit of less clarity among peaks. From these observations, we can see that the primary impact of disorder on the two-phonon structure is manifested by the broadening of peaks and the projection of the PDOS. Furthermore, the persistence of the two-phonon structure across doped samples suggests that disorder does not hinder the electron-phonon coupling. This corollary aligns with previous observations regarding the $1/|q|$ parameter of the E_{2g}^{2} mode.

Our results reveal the origin of two-phonon structures in the $2H$-$TaSe_{2-x}S_x$ compounds. It is also evident that, although disorder does not directly influence the strength of the EPC (in

the range from $x = 0.25$ to 1.65), it affects the phenomena that share EPC as a seemingly common origin differently. While the CDW is destroyed, SC and the two-phonon structure survive [17] suggesting that strong EPC alone is insufficient to sustain the CDW in a disordered lattice. It is interesting to note that these materials simultaneously and independently experience the effects of disorder and EPC.

IV. CONCLUSIONS

In this study, we conducted a Raman scattering analysis of $2H$-$TaSe_{2-x}S_x$ ($0 \leqslant x \leqslant 2$) alloys. The Raman spectra of the end compounds host two out of the three symmetry-expected Raman active modes for backscattering configuration and an additional peak O_1 of A_{1g} symmetry, present only in the $2H$-TaS_2 spectra. This O_1 peak is a result of second-order Raman scattering, overtone in nature, observable due to the prominent EPC, characteristic for CDW materials. The broad two-phonon structures observed in pristine samples were linked to enhanced EPC in the corresponding phonon branches, as obtained from our first-principles calculations. The gradual substitution of Se atoms with S atoms results in crystallographic disorder, introducing new scattering channels—in the form of an additional peak P_1 of A_{1g} symmetry, as well as PDOS projection and broadening of all phonon modes. Dependence on sulfur content showed hardening of all modes, except for E^2_{2g} mode. Softening of the E^2_{2g} mode and its discontinuous dependence were attributed to strong EPC. Coexistence of A_{1g} peaks in intermediate doping levels arises probably due to nanoscale clusters comprised mainly of either Se or S atoms. In spectra where disorder reaches its maximum, four single-phonon peaks accompanied the background two-phonon structure, with energies corresponding to the region of PDOS maxima. The negligible influence of disorder on the EPC was supported by the continued presence of the two-phonon structure and the behavior of the $1/|q|$ parameter associated with the E^2_{2g} mode. Thus, in the absence of changes in either electron-electron [17] or EPCs, significant rise of T_{SC} in doped alloys is only due to disorder-induced CDW suppression. Our findings provide insights into the intricate relationship between disorder and EPC, shedding light on their combined influence in governing the vibronic and collective electronic behavior of $2H$-$TaSe_{2-x}S_x$ compounds.

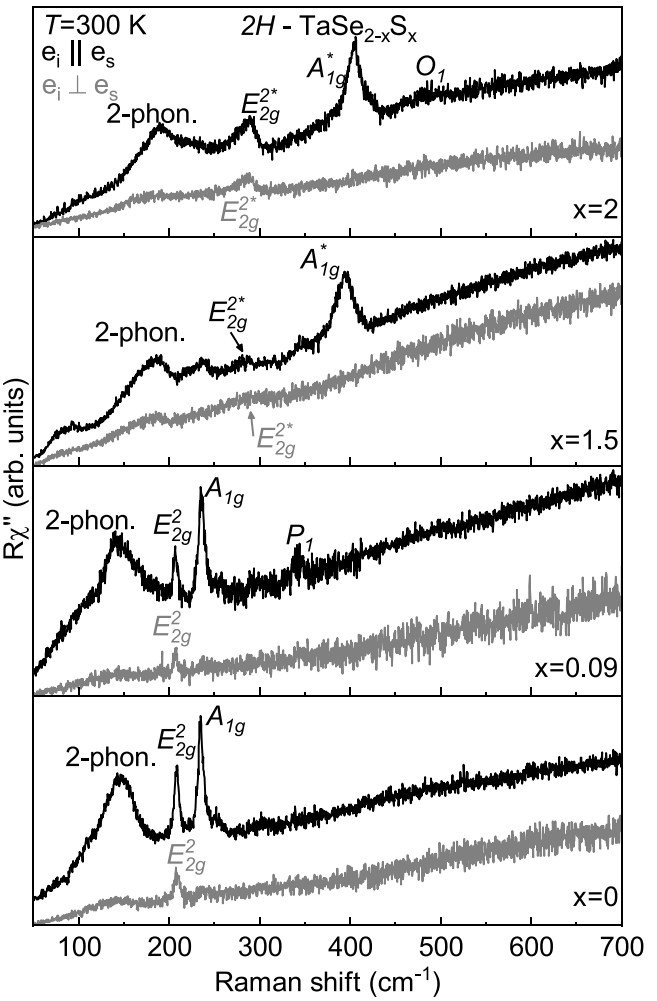

FIG. 5. Raman response of $2H$-$TaSe_2$, $2H$-$TaSe_{1.5}S_{0.5}$, $2H$-$TaSe_{1.91}S_{0.09}$, and $2H$-TaS_2 for parallel (black) and crossed (gray) polarization configurations at $T = 300$ K. The possible overtone modes O_1 and P_1 are only present in parallel polarization configuration.

ACKNOWLEDGMENTS

Authors J. Blagojević and S. Djurdjić Mijin contributed equally to the paper. The authors acknowledge funding provided by the Institute of Physics Belgrade through the grant by the Ministry of Science, Technological Development and Innovation of the Republic of Serbia, Project No. F-134 of the Serbian Academy of Sciences and Arts, the Science Fund of the Republic of Serbia, PROMIS, No. 6062656, StrainedFeSC, and by Research Foundation-Flanders (FWO). J. Bekaert acknowledges support as a Senior Postdoctoral Fellow of the FWO (Fellowship No. 12ZZ323N), and from the Erasmus+ program for staff mobility and training (KA107, 2018) for a research stay at the Institute of Physics Belgrade, during which part of this work was carried out. The computational resources and services used for the first-principles calculations in this work were provided by the VSC (Flemish Supercomputer Center), funded by the FWO and the Flemish Government-department EWI. Work at Brookhaven National Laboratory was supported by U.S. DOE, Office of Science, Office of Basic Energy Sciences under Contract No. DE-SC0012704. The authors are grateful for the support by the European Cooperation in Science and Technology COST Action No. CA21144 (SUPERQUMAP), Superconducting Nanodevices and Quantum Materials for Coherent Manipulation, by the Vinca Institute of Nuclear Sciences (Contract No. 451-03-66/2024-03/200017, by the Shanghai Key Laboratory of Material Frontiers Research in Extreme Environments, China (No. 22dz2260800) and Shanghai Science and Technology Committee, China (No. 22JC1410300)

APPENDIX A: MODE ASSIGNATION AND NATURE OF ADDITIONAL PEAKS

Raman spectra of all samples were measured in parallel and crossed polarization configurations in order to correctly

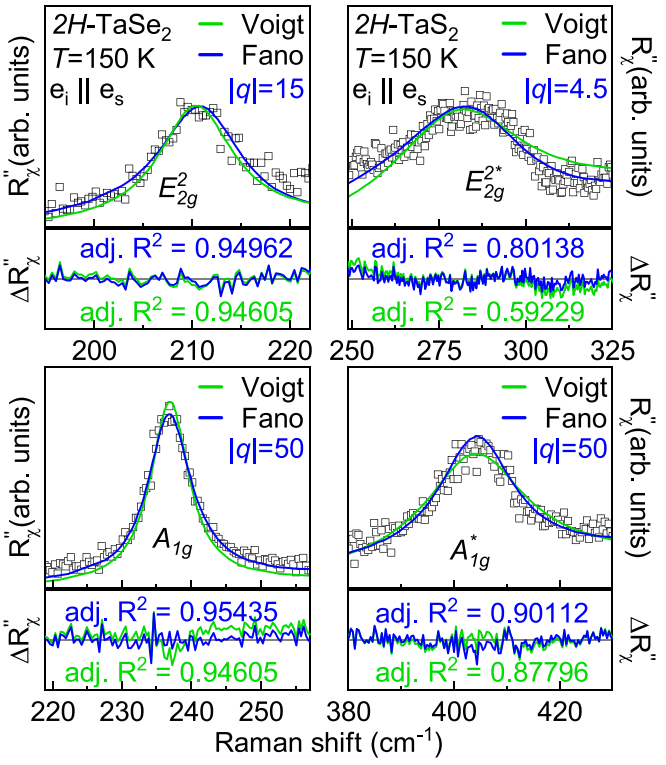

FIG. 6. Raman response as a function of the Raman shift. Quantitative analysis of the E^2_{2g}, E^{2*}_{2g}, A_{1g}, and A^*_{1g} modes at $T = 150$ K. The blue and green solid lines represent Fano and Voigt profiles fitted to the experimental data, respectively. Experimental data is represented by open squares.

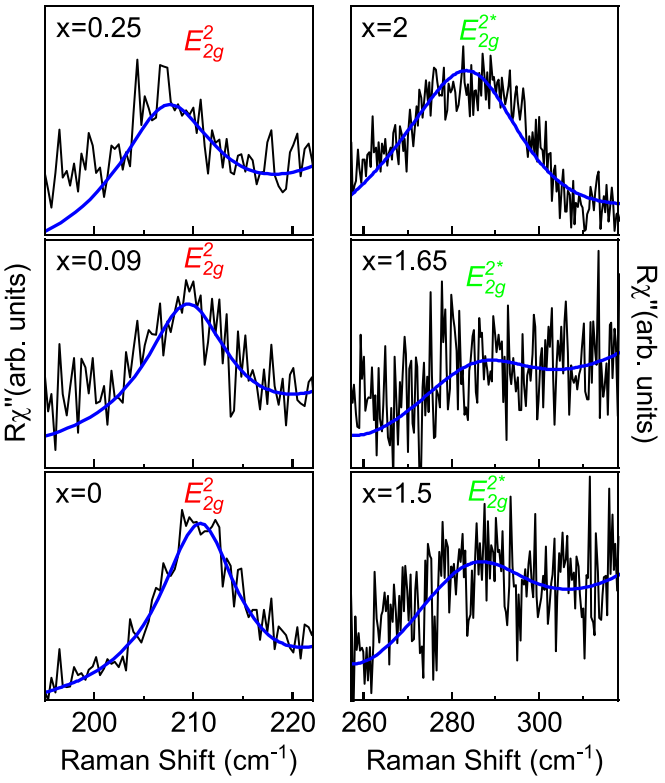

FIG. 7. Raman response as a function of the Raman shift. Quantitative analysis of the E^2_{2g} and E^{2*}_{2g} modes for indicated sulfur content x in the measured crystals. The blue lines represent Fano profiles fitted to the experimental data.

assign theoretically predicted modes as well as the unexpected and additional peaks and structures. From the Raman spectra presented in Fig. 5 theoretically predicted A_{1g} and E^2_{2g} modes were easily identified. Given that the O_1 and P_1 peaks are only present in parallel polarization configuration, they obey pure A_{1g} symmetry rules. Two-phonon structure is present in both polarization configurations, but with significantly higher intensity in A_{1g} channel. Additional features in two-phonon structure in the spectra of $2H$-$TaSe_{1.5}S_{0.5}$ are only present in parallel polarization configuration, thus they are possibly overtones in nature or single-phonon excitations of A_{1g} symmetry.

APPENDIX B: FITTING DETAILS

All peaks were fitted using both asymmetric Fano profiles and symmetric Voigt profiles. Since the line widths of the analyzed phonon modes were much greater than the resolution of spectrometer σ, the real width of the peaks could be obtained without the need to use Fano profiles convoluted with a Gaussian function, where $\Gamma_L = \sigma$. The comparison between the obtained fits are presented in Fig. 6. As it can be seen, peaks E^2_{2g} and E^{2*}_{2g} show clear asymmetric line shape, whereas the A_{1g} symmetry peaks do not. Therefore, the latter were fitted with Fano parameter value $|q|$ being fixed at 50. Acquired phonon parameters as a function of sulfur content x are presented in Fig. 4. The increase in doping leads to the significant decrease in the relative intensity of E^2_{2g} Raman active modes, therefore the obtained phonon parameters have slightly higher error bar compared to the A_{1g} modes. Fits obtained using Fano profiles in the energy range of peaks E^2_{2g} and E^{2*}_{2g} are presented in Fig. 7. The two-phonon structure interferes with the lower energy side of the peaks in the spectra of all doped samples, contributing to the mentioned error.

[1] K. S. Novoselov, A. Mishchenko, A. Carvalho, and A. H. C. Neto, 2D materials and van der Waals heterostructures, Science **353**, aac9439 (2016).

[2] J. A. Wilson and A. D. Yoffe, The transition metal dichalcogenides discussion and interpretation of the observed optical, electrical and structural properties, Adv. Phys. **18**, 193 (1969).

[3] A. H. Castro Neto, Charge density wave, superconductivity, and anomalous metallic behavior in 2D transition metal dichalcogenides, Phys. Rev. Lett. **86**, 4382 (2001).

[4] X. Yin, C. S. Tang, Y. Zheng, J. Gao, J. Wu, H. Zhang, M. Chhowalla, W. Chen, and A. T. S. Wee, Recent developments in 2D transition metal dichalcogenides: phase transition and applications of the (quasi-)metallic phases, Chem. Soc. Rev. **50**, 10087 (2021).

[5] Q. H. Wang, K. Kalantar-zadeh, A. Kis, J. Coleman, and M. Strano, Electronics and optoelectronics of two-dimensional transition metal dichalcogenides, Nat. Nanotechnol. **7**, 699 (2012).

[6] F. Zheng and J. Feng, Electron-phonon coupling and the coexistence of superconductivity and charge-density wave in monolayer $NbSe_2$, Phys. Rev. B **99**, 161119(R) (2019).

[7] Y. Kvashnin, D. VanGennep, M. Mito, S. A. Medvedev, R. Thiyagarajan, O. Karis, A. N. Vasiliev, O. Eriksson, and M. Abdel-Hafiez, Coexistence of superconductivity and charge density waves in tantalum disulfide: Experiment and theory, Phys. Rev. Lett. **125**, 186401 (2020).

[8] Y. Liu, L. J. Li, W. J. Lu, R. Ang, X. Z. Liu, and Y. P. Sun, Coexistence of superconductivity and commensurate charge density wave in 4Hb-$TaS_{2-x}Se_x$ single crystals, J. Appl. Phys. **115**, 043915 (2014).

[9] J. A. Holy, M. V. Klein, W. L. McMillan, and S. F. Meyer, Raman-active lattice vibrations of the commensurate superlattice in 2*H*-$TaSe_2$, Phys. Rev. Lett. **37**, 1145 (1976).

[10] S. Sugai, K. Murase, S. Uchida, and S. Tanaka, Studies of lattice dynamics in 2*H*-TaS_2 by Raman scattering, Solid State Commun. **40**, 399 (1981).

[11] S. Sugai and K. Murase, Generalized electronic susceptibility and charge-density waves in 2*H*-$TaSe_2$ by Raman scattering, Phys. Rev. B **25**, 2418 (1982).

[12] D. B. McWhan, R. M. Fleming, D. E. Moncton, and F. J. DiSalvo, Reentrant lock-in transition of the charge-density wave in 2*H*-$TaSe_2$ at high pressure, Phys. Rev. Lett. **45**, 269 (1980).

[13] P. Hajiyev, C. Cong, C. Qiu, and T. Yu, Contrast and Raman spectroscopy study of single-and few-layered charge density wave material: 2*H*-$TaSe_2$, Sci. Rep. **3**, 2593 (2013).

[14] M. Lee, M. Šiškins, S. Mañas-Valero, E. Coronado, P. G. Steeneken, and H. S. J. van der Zant, Study of charge density waves in suspended 2*H*-TaS_2 and 2*H*-$TaSe_2$ by nanomechanical resonance, Appl. Phys. Lett. **118**, 193105 (2021).

[15] S. Behera and G. Mohanty, Theory of two-phonon modes in layered charge-density-wave systems, Pramana **26**, 239 (1986).

[16] J. Joshi, H. M. Hill, S. Chowdhury, C. D. Malliakas, F. Tavazza, U. Chatterjee, A. R. Hight Walker, and P. M. Vora, Short-range charge density wave order in 2*H* −TaS_2, Phys. Rev. B **99**, 245144 (2019).

[17] L. Li, X. Deng, Z. Wang, Y. Liu, M. Abeykoon, E. Dooryhee, A. Tomic, Y. Huang, J. B. Warren, E. S. Bozin, S. J. L. Billinge, Y. Sun, Y. Zhu, G. Kotliar, and C. Petrovic, Superconducting order from disorder in 2*H*-$TaSe_{2-x}S_x$, npj Quantum Mater. **2**, 11 (2017).

[18] J. Peng, Z. Yu, J. Wu, Y. Zhou, Y. Guo, Z. Li, J. Zhao, C. Wu, and Y. Xie, Disorder enhanced superconductivity toward TaS_2 monolayer, ACS Nano **12**, 9461 (2018).

[19] J. Bekaert, E. Khestanova, D. G. Hopkinson, J. Birkbeck, N. Clark, M. Zhu, D. A. Bandurin, R. Gorbachev, S. Fairclough, Y. Zou, M. Hamer, D. J. Terry, J. J. P. Peters, A. M. Sanchez, B. Partoens, S. J. Haigh, M. V. Milošević, and I. V. Grigorieva, Enhanced superconductivity in few-layer TaS_2 due to healing by oxygenation, Nano Lett. **20**, 3808 (2020).

[20] X. Gonze, B. Amadon, G. Antonius, F. Arnardi *et al.*, The Abinit project: Impact, environment and recent developments, Comput. Phys. Commun. **248**, 107042 (2020).

[21] S. Goedecker, M. Teter, and J. Hutter, Separable dual-space Gaussian pseudopotentials, Phys. Rev. B **54**, 1703 (1996).

[22] M. Krack, Pseudopotentials for H to Kr optimized for gradient-corrected exchange-correlation functionals, Theor. Chem. Acc. **114**, 145 (2005).

[23] X. Gonze, D. C. Allan, and M. P. Teter, Dielectric tensor, effective charges, and phonons in α-quartz by variational density-functional perturbation theory, Phys. Rev. Lett. **68**, 3603 (1992).

[24] A. Mialitsin, Fano line shape and anti-crossing of Raman active E_{2g} peaks in the charge density wave state of $NbSe_2$, J. Phys. Chem. Solids **72**, 568 (2011).

[25] A. Baum, A. Milosavljević, N. Lazarević, M. M. Radonjić, B. Nikolić, M. Mitschek, Z. I. Maranloo, M. Šćepanović, M. Grujić-Brojčin, N. Stojilović, M. Opel, A. Wang, C. Petrovic, Z. V. Popović, and R. Hackl, Phonon anomalies in FeS, Phys. Rev. B **97**, 054306 (2018).

[26] V. B. Podobedov, A. Weber, D. B. Romero, J. P. Rice, and H. D. Drew, Effect of structural and magnetic transitions in $La_{1-x}M_xMnO_3$ (m = Sr, Ca) single crystals in Raman scattering, Phys. Rev. B **58**, 43 (1998).

[27] I. Charrier-Cougoulic, T. Pagnier, and G. Lucazeau, Raman spectroscopy of perovskite-type $BaCe_xZr_{1-x}O_3 (0 \leqslant x \leqslant 1)$, J. Solid State Chem. **142**, 220 (1999).

[28] S. Issing, A. Pimenov, V. Y. Ivanov, A. A. Mukhin, and J. Geurts, Composition-dependent spin-phonon coupling in mixed crystals of the multiferroic manganite $Eu_{1-x}Y_xMnO_3 (0 \leqslant x \leqslant 0.5)$ studied by Raman spectroscopy, Phys. Rev. B **81**, 024304 (2010).

[29] U. Fano, Effects of configuration interaction on intensities and phase shifts, Phys. Rev. **124**, 1866 (1961).

[30] V. G. Sathe, S. Tyagi, and G. Sharma, Electron-phonon coupling in perovskites studied by Raman scattering, J. Phys.: Conf. Ser. **755**, 012008 (2016).

[31] S. Nimori, S. Sakita, F. Nakamura, T. Fujita, H. Hata, N. Ogita, and M. Udagawa, Electron-phonon interaction in $La_{2-x}Sr_xCuO_4$ investigated by Raman scattering, Phys. Rev. B **62**, 4142 (2000).

[32] N. Lazarević, Z. V. Popović, R. Hu, and C. Petrovic, Evidence for electron-phonon interaction in $Fe_{1-x}M_xSb_2$ (M=Co and Cr) $(0 \leqslant x \leqslant 0.5)$ single crystals, Phys. Rev. B **81**, 144302 (2010).